 CMC, vol.1, no.2, pp.173-190, 2004

Stress Concentrations Caused by Embedded Optical Fiber Sensors in Composite Laminates

Kunigal Shivakumar[1] **and Anil Bhargava**[2]

Abstract: The fiber optic sensor (FOS) embedded perpendicular to reinforcing fibers causes an 'Eye' shaped defect. The length is about 16 times fiber optic radius (R_{FOS}) and height is about $2R_{FOS}$. The eye contains fiber optics in the center surrounded by an elongated resin pocket. Embedding FOS causes geometric distortion of the reinforcing fiber over a height equal to 6 to 8 R_{FOS}. This defect causes severe stress concentration at the root of the resin pocket, the interface (in the composite) between the optical fiber and the composite, and at 90 ^{o} to load direction in the composite. The stress concentration was calculated by finite element modeling of a representative micrograph. The FE results agreed reasonably with analytical and experimental data in the literature for a similar problem. The stress concentration in axial direction was about 1.44 and in transverse direction at the interface was -0.165 and at resin pocket was 0.171. Under tensile loading, the initial failure was by transverse matrix cracking (fiber splitting) at the root of the resin pocket, then that lead to final fracture by fiber breakage. Under compression loading, the failure initiation was by interfacial cracking due to large transverse tensile stress and the final fracture was by compression. Fracture stress calculated from the analysis using the maximum stress criteria agreed reasonably with test data.

keyword: Composite Material, Optical Fiber Sensor, Stress Concentration, Failure Mechanics, Finite Element Model, Eye Shaped Defect

1 Introduction

A majority of the health monitoring technologies used today started as techniques to identify and suppress undesirable vibrations in space structures and helicopter components. The sensory methods included dielectric, electrical impedance, vibrations, ultrasonic, piezoelectric, shape-memory alloys, fiber optics, peak strain sensors, embedded MEMS and so forth. Most of these sensors were used as non-contact and/or surface mounted devices and many of them were not suitable for continuous on-line health monitoring. A promising technology is the fiber optic sensor (FOS) because of its ability to embed in composite materials. Optical fibers are relatively small (100-200μm), lightweight, resistant to corrosion and fatigue, immune to electromagnetic interference and are reasonably compatible with composites. However, the FOS diameter (100-200μm), about a ply thickness, is not small when compared to the reinforcing fibers (5-10μm) in composites. In order for embedded FOS composite structures to be accepted, it must be shown that FOS inclusion does not lead to degradation of structural properties.

A number of experimental studies [Claus, Bennet, and Jackson (1985), Udd, et al (1987), Shelly (1988), Jensen and Griffiths (1988), Measure (1989), Yarcho (1989), Jensen, Pascaul and August (1992a and 1992b), Roberts and davidson (1992), Holl and Boyd (1993), Emmanwori and Shivakumar (2002), Emmanwori (2002), Shivakumar and Emmanwori (2002), Roberts and Davidson (1991)] have been conducted on embedded FOS in unidirectional, cross ply and quasi-isotropic laminates subjected to tensile, compressive and fatigue loads. The FOS orientations were both parallel and perpendicular to reinforcing fibers. These studies showed that embedded FOS has caused almost no loss of tensile modulus, 10-20% loss of tensile strength and a significant reduction in compressive strength (up to 40%). These results are summarized in Fig. 1.

A number of analytical studies [Waite and Sage (1988), Salehi et al (1989), Mathews and Sirkis (1990), Davidson (1992), Pak, DyReyes and Schumuter (1992), Jensen, Pascaul and August (1992c)] were made on embedded

[1] Research Professor and Director, Center for Composite Materials Research, Department of Mechanical Engineering, North Carolina A&T State University, Greensboro, NC 27411

[2] Graduate Student, Center for Composite Materials Research, North Carolina A&T State University, Greensboro, NC 27411

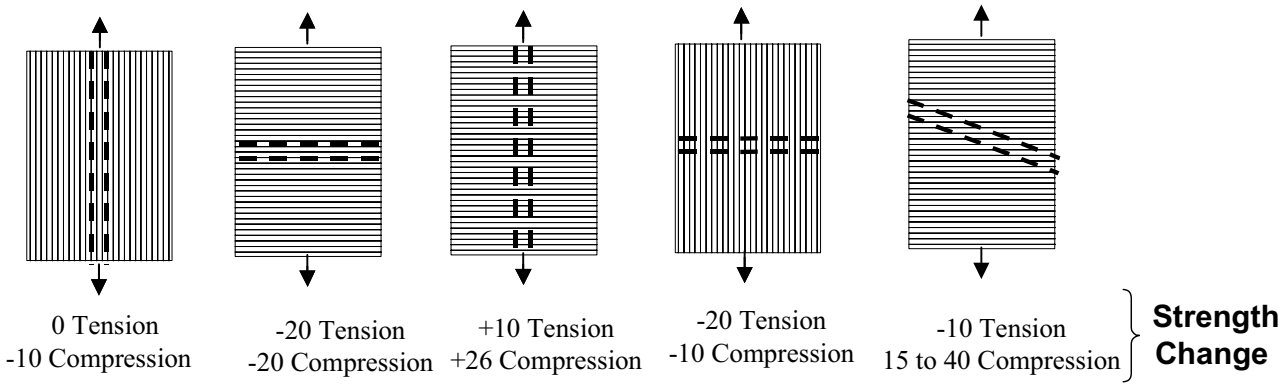

Figure 1 : Strength Reductions Due to FOS Orientation (Broken cylinders represent the fiber optic sensor)

optical fiber in composite laminate subjected to tensile, shear and thermal loads. A majority of these papers [Waite and Sage (1988), Pak, DyReyes and Schumuter (1992), Dasgupta et al (1990), Carman and Reifsneider (1992)] were based on concentric cylindrical model to examine strain concentration at the interface of the optical fiber, optimization of coating material properties to reduce strain concentration, and failure of optical fibers. Salehi etal (1989), Mathews and Sirkis (1990) and Davidson (1992) used lenticular model and finite element analysis to study stresses around the coated optical fiber embedded in the composites. They assumed the composite to be homogeneous and orthotropic but ignored the fiber geometric distortion caused by the optical fiber.

The primary objective of this research paper is to consider the fiber waviness or the distortion caused by the embedment of FOS in unidirectional composite laminate and to assess its impact on local stresses/strains and potential failure modes. The specific objectives are to assess the effect of defect caused by embedment of optical fiber sensor by accurate modeling of the problem; to assess the effect of size of the defect in terms of fiber disturbance height and resin pocket length; and to investigate the effect of the residual curing stresses.

2 Modeling of Defect Caused by FOS Embedment

Figure 2 shows a micrograph [Emmanwori and Shivakumar (2002), Emmanwori (2002)] of the cross-section of an 8-ply unidirectional laminate embedded with an optical fiber, which is perpendicular to the reinforcing fibers. The laminate is AS4/3501-6 composite and the diameter of the optical fiber with the polyamide coating is 128/145 μm. The fibers flow over the optical fiber forming an "eye" shaped defect. This eye contains a resin matrix, separated while processing the composite and the optical fiber. Sometimes a void is also formed (See Fig.2), which is ignored in the present study. This resin pocket causes stress and strain concentration in and around the optical fiber and forms a potential site for damage initiation, such as matrix cracks, which may lead to delamination. Further, the geometric distortion of the fibers also influences the local stress distribution.

Shapes and sizes of the resin pocket region were measured from the micrographs taken for a number of 90 ^{o} oriented optical fiber in 8 and 16 ply laminates [Emmanwori and Shivakumar (2002), Emmanwori (2002), Shivakumar and Emmanwori (2002)]. An average size was evolved and the idealized symmetric model, retaining all critical features, is shown in Fig. 3. Stress concentrations under tensile and compression loading are investigated.

3 Failure Hypotheses

Through the experimental study, Shivakumar and Emmanwori (2002) developed a hypothesis for failure of FOS embedded composite under tension and compression loading. These hypotheses are presented here and verified later.

3.1 Tension Load

In composite laminates with off-axis (or 90 ^{o}) embedded FOS, the failure initiates as fiber-matrix split at the root of the resin pocket (location A, see Fig. 4 (a) because of high transverse stresses. This split grows upon continued loading and then stops. Finally, the specimen fails

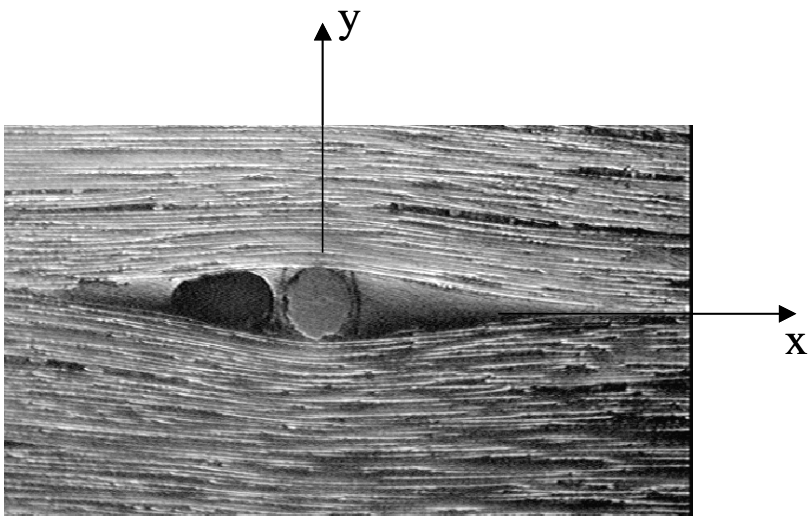

Figure 2 : Micrograph of section of composite laminate embedded with FOS

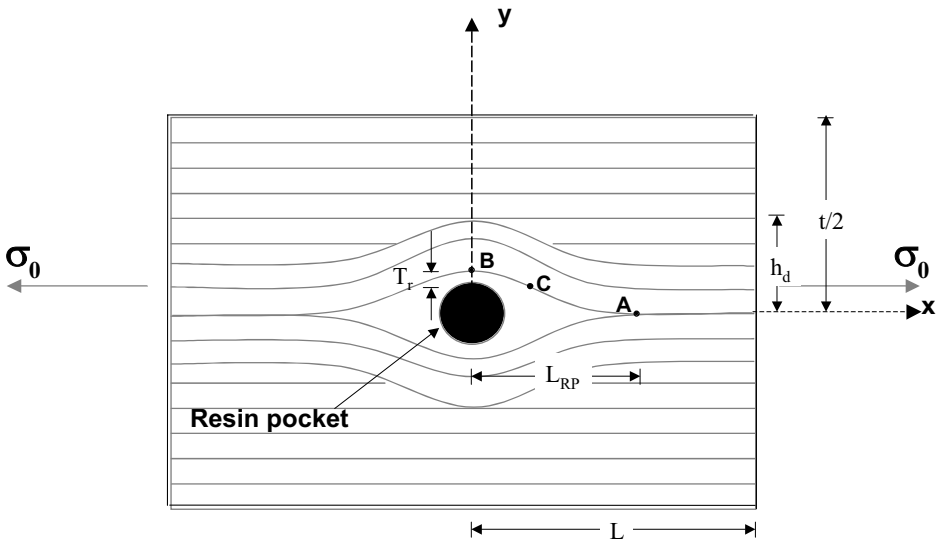

Figure 3 : Idealized model

by fiber breakage as in Fig. 4 (d). Figure 4 shows critical stress locations, failure initiation as fiber-matrix separation, its growth and final fracture. Axial loading causes transverse stresses at A due to geometric disturbance of reinforcing fibers. Stresses are tensile (compressive) at A while they are compressive (tensile) at B (interface between the optical fiber and the composite) under tension (compression) loading. In addition, there is an axial stress concentration at B within the composite. The transverse tensile stress could exceed the transverse tension strength of the composite, before any other failure occurs, causing the fiber-matrix split at A. The split relieves the axial stress concentration at B (within the composite) leading, finally, to a tensile fiber breakage.

3.2 Compression Load

Figure 5 describes the failure process. Under compression loading, high transverse tensile stresses are created at B (at any one or both locations), which cause interfacial cracking between FOS and the composite. Then, the crack propagates to resin pocket root (A), causing increased misalignment of the reinforcing fibers. As

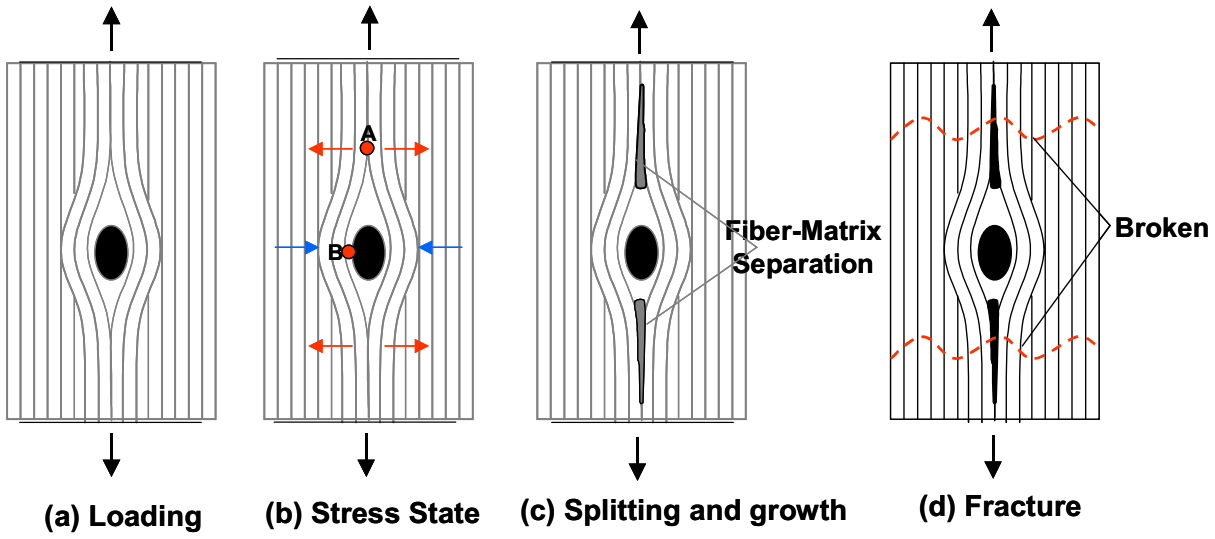

Figure 4 : Tensile Failure Process for Composite Laminate Embedded with Optical Fiber at 90 ^{o} to the Load Axis [Emmanwori (2002), Shivakumar and Emmanwori (2002)]

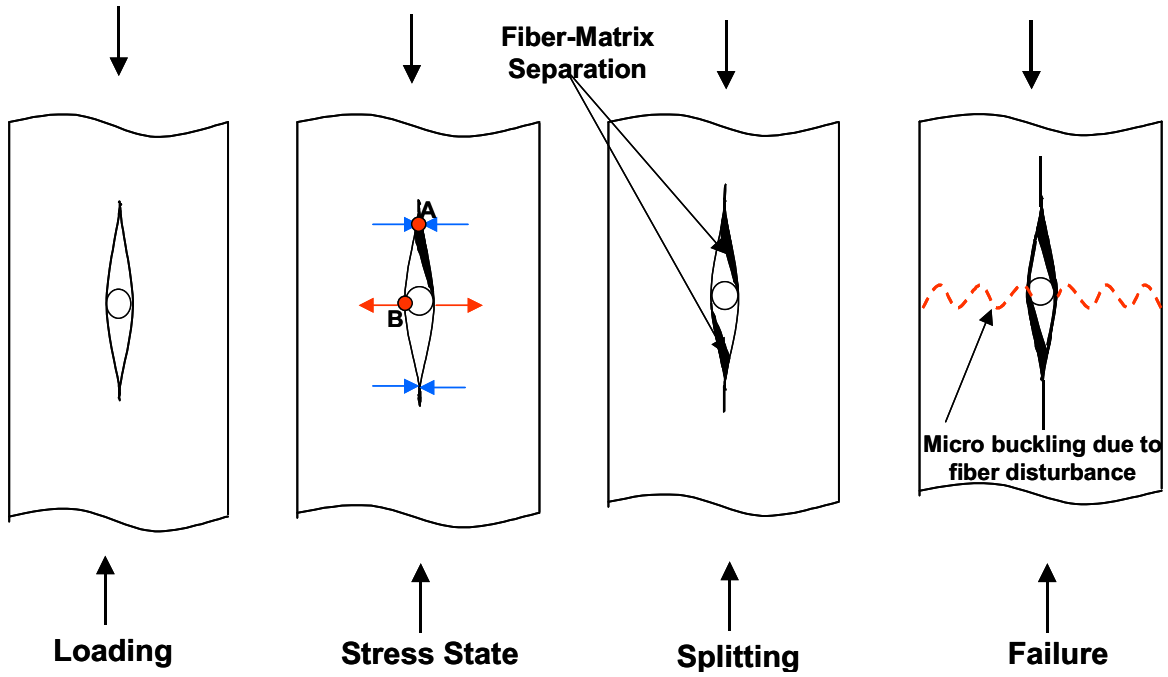

Figure 5 : Compression Failure Process for Composite Laminate Embedded with Optical Fiber at 90 ^{o} to the Load Axis [Emmanwori (2002), Shivakumar and Emmanwori (2002)]

noted in references [Emehel and Shivakumar (1997), Budiansky (1983), Budiansky and Fleck (1993)], compression strength is a function of the angle of fiber misalignment. Finally the specimen breaks by fiber micro-buckling/kinking. Unlike the tensile loading case, interfacial crack propagation does not alter the axial stress concentration. Post-failure analysis of the specimen revealed that the final failure was by fiber micro-buckling/kinking.

Table 1a : Mechanical properties of the optical fiber/host system

Material	Young's Modulus GPa			Shear Modulus GPa		Poisson's ratio	
	E_x	E_y	E_z	Gxy	Gyz	ν_{xy}	ν_{yz}
Silica Glass Core (Optical fiber)	72.90	72.90	72.90	31.10	31.10	0.17	0.17
Polyimide Coating	2.00	2.00	2.00	0.74	0.74	0.35	0.35
3501-6 Epoxy Matrix (Resin pocket)	1.72	1.72	1.72	0.25	0.25	0.35	0.35
Carbon/epoxy (AS4/3501-6)	142.00	10.30	10.30	7.20	4.12	0.27	0.25

Table 1b : Thermal properties

Material	α_1 ($* 10^{-6}$/°F)	α_2 ($* 10^{-6}$/°F)
Silica Glass Core (Optical fiber)	0.417	0.417
Polyimide Coating	28.000	28.000
3501-6 Epoxy Matrix (Resin pocket)	50.000	50.000
Carbon/epoxy (AS4/3501-6)	-0.500	15.000

4 Modeling of the Defect

All the geometric parameters in Fig.3 are normalized by the optical fiber radius R_{FOS}. The R_{FOS} includes optical fiber and cladding. The resin pocket region's half-length, L_{RP} is about $8R_{FOS}$ and the coating radius is about $1.06R_{FOS}$. The parameter, $L_{RP}= 8R_{FOS}$, is considered as the baseline with which all other L_{RP} solutions are compared. The height, h_d, the region over which the reinforcing fiber, disturbed from axiality, is shown in Fig. 6. The parameter, h_d, measured from the micrographs is about $3.12R_{FOS}$, which is considered as the baseline with which all other h_d solutions will be compared. The analysis is performed for h_d values ranging from 2.5 to 5.0 to assess its effect on local stress concentration.

The symmetric quarter of the model is shown in Fig. 6. The different areas having different material properties are identified in Fig. 7. The curved lines in Fig. 6 represent the profile of the reinforcing fibers, which are geometrically distributed as per the micrograph. Although the gage length of the test specimen was 6-inch, the model length is restricted to $96\ R_{FOS}$ (or 6 times the resin pocket length). Tables 1a and 1b list elastic and thermal properties of optical fiber (Area1), coating (Area2), resin pocket (Area3) and composites (Area4 and Area5). In Area5, fiber angle was varied to follow the shape of the resin pocket and gradually change parallel to the x-axis.

5 Analytical Solution – Circular Elastic Inclusion in an Orthotropic Plate

A general solution to a circular elastic inclusion in a wide orthotropic rectangular plate subjected to tension loading is presented in Lekhnitskii's book on composite laminates (1975). Stress concentration factor to the problem of isotropic glass fiber inclusion in a wide AS4/3501-6 orthotropic material (0^o) was obtained using the properties in Table 1a. The tensile stress concentration factor at B (See Fig.3) was found to be 1.71.

6 Finite Element Analysis

6.1 Modeling

The model geometry (Fig.3) and the loading were symmetric, hence only one quarter of the model was used. The specimen width was very large compared to its thickness; hence, the model was assumed to be in a plane strain state. The center of optical fiber was taken as the origin. The length, the width and thickness directions were taken as x, y and z-axes, respectively. Figure 7 shows an x-y section of the model with different material areas identified and the boundary conditions.

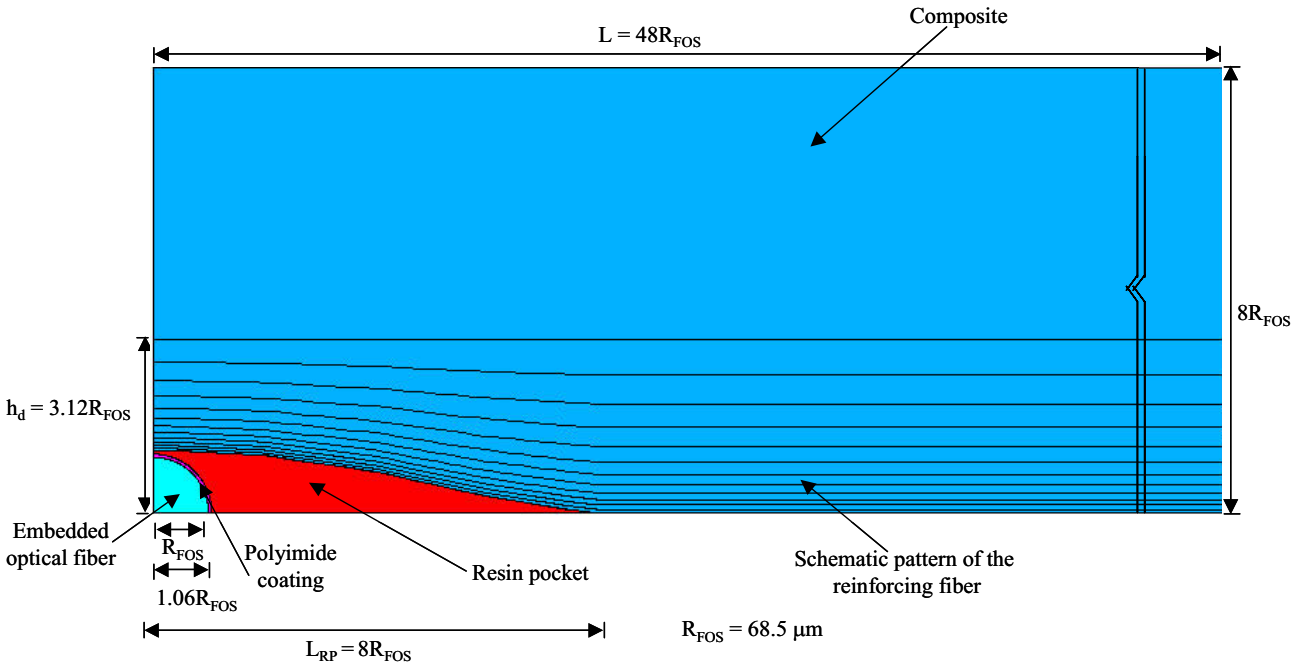

Figure 6 : One-quarter of the idealized model

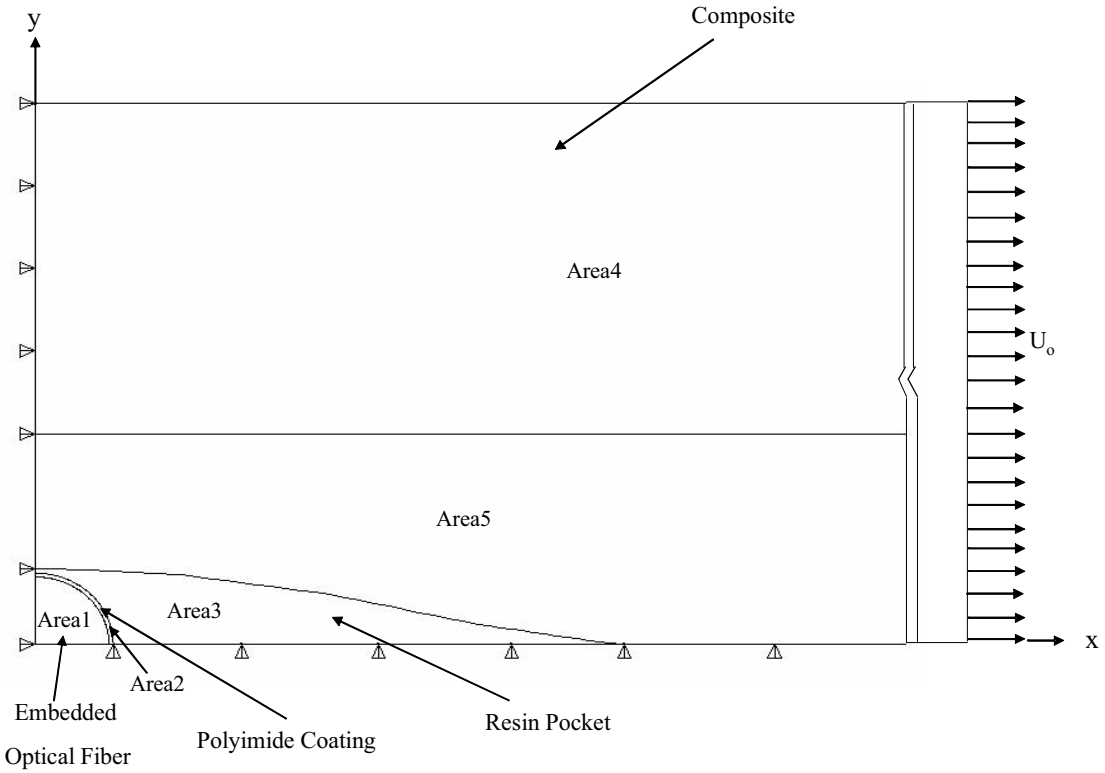

Figure 7 : Descritization of various regions

The regions in Fig. 7 were modeled using four-noded quadrilateral elements (plane 42) using a commercial finite element code ANSYS Version 5.6. The mesh generation of the code was used to descretize the line boundary into a different number of parts. The isoparametric mapping concept was used to map the model using quadrilateral elements. The line divisions and grading were carefully chosen so that the stress gradients were captured accurately. The areas were modeled using the IJKL option available in ANSYS. This option allows the profile of elements and fibers in Area5 to follow parallel to inclusion and slowly become straight past the resin pocket region. This is particularly important to reduce the material data preparation and capture a smooth profile of the fibers transition to straight line at the end of the resin pocket. Several coarse mesh analyses were conducted to evaluate the convergence of the results. The finite element mesh shown in Fig. 8 is the converged solution mesh. The model around the optical fiber region is enlarged and shown separately. The model had 3,724 elements, 3,861 nodes and 7,547 degrees-of-freedom.

6.2 Analysis

Symmetry boundary conditions are imposed by constraining y-direction displacement on the x-axis and x-displacement on the y-axis. The end x = L (=$48R_{FOS}$) was loaded by uniform displacement in x equivalent to 1% strain. Linear elastic analysis was conducted and complete displacement, strain, and stress fields were calculated. Reactions at the end of the model (x = $48R_{FOS}$) were summed and the average stress (σ_o= 1.404 GPa) at this section was obtained. This remote stress can also be calculated from the 3-D constitutive equations for plane-strain condition ignoring the local effect (fiber optics region). This equation reduces to $\sigma_0 = \frac{\varepsilon_x E_x}{1-\nu_{xz}\nu_{zx}}$, $Note$; $\nu_{xz} = \nu_{xy}$. By substituting the properties in Table 1a for the carbon-epoxy we get σ_0 = 1.5, which is slightly higher than the FE results because of ignoring the flexibility introduced by soft defect and distortion of fiber. This further verifies the fidelity of the FE modeling. First results for the baseline case (h_d= $3.12R_{FOS}$ and L_{RP} =$8R_{FOS}$) are presented and then the results of the parametric studies will be summarized.

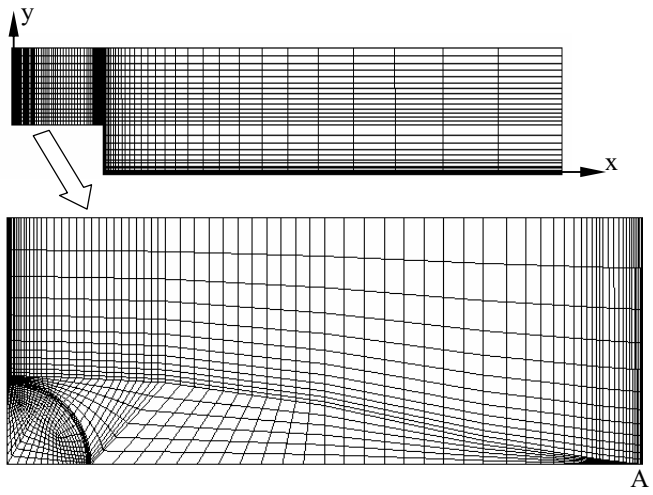

Figure 8 : Global and local finite mesh at critical locations

7 Results and Discussion

7.1 Baseline Case

The geometric parameters of the baseline case are resin pocket length, L_{RP}= $8R_{FOS}$, fiber disturbance height h_d = $3.12R_{FOS}$ and transition resin layer thickness T_r = 0.06. The baseline model is same as the measurements made on the micrograph [Mathews and Sirkis (1990)].

7.1.1 Strain and Stress Field

The plane strain condition of the problem results in only two principal strains ε_1 and ε_2. Figures 9 and 10 show maximum (ε_1) and minimum (ε_2) principal strain contours respectively. Both local and global regions are shown. Maximum principal strain concentration is at A (at the root of the resin pocket), which is about 7.9 while Czarnek et al. (1989) measured 14.2 by the Moire interferometry technique. The high strain gradient and the geometry of the resin region clearly depicts that location A is a "singular point". Before the composite fractures at A, the resin may yield or may break away from the rest of the composite. Therefore, this could be a potential site for failure initiation. The minimum principal transverse strain (ε_2) concentration is also near A (but not at A) and is about 0.83. The longitudinal strain at B is about 1.0 %, not far from the remote strain.

Figures 11 and 12 show the principal stress (σ_1 and σ_2) contours of the model. All stresses are in GPa for

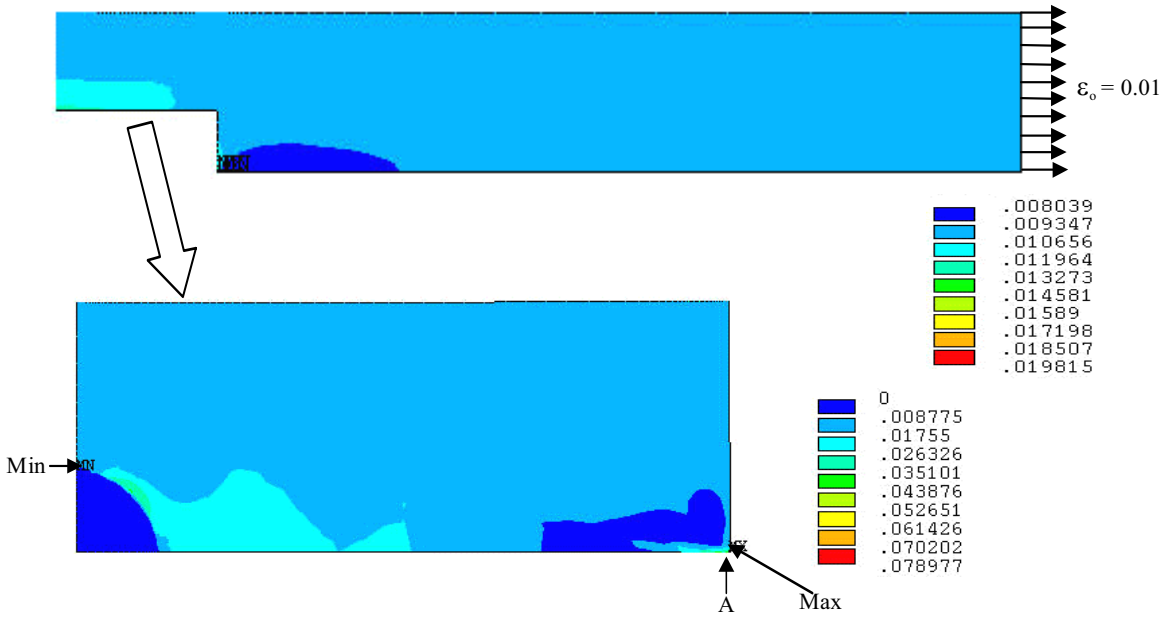

Figure 9 : Maximum principal (ε_1) strain contours (global and local views)

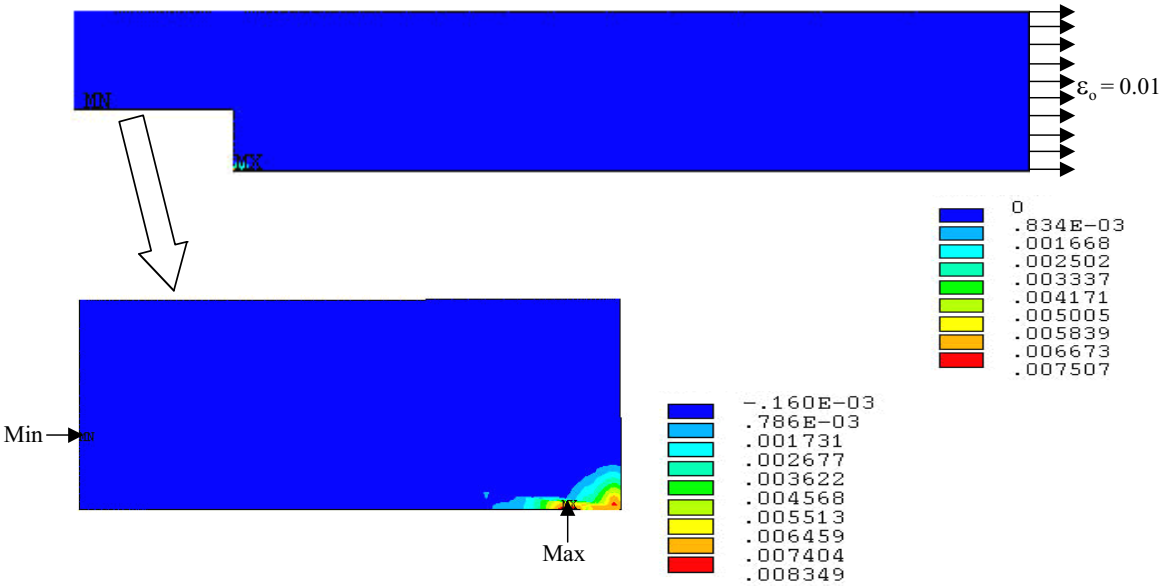

Figure 10 : Minimum principal (ε_2) strain contours (global and local views)

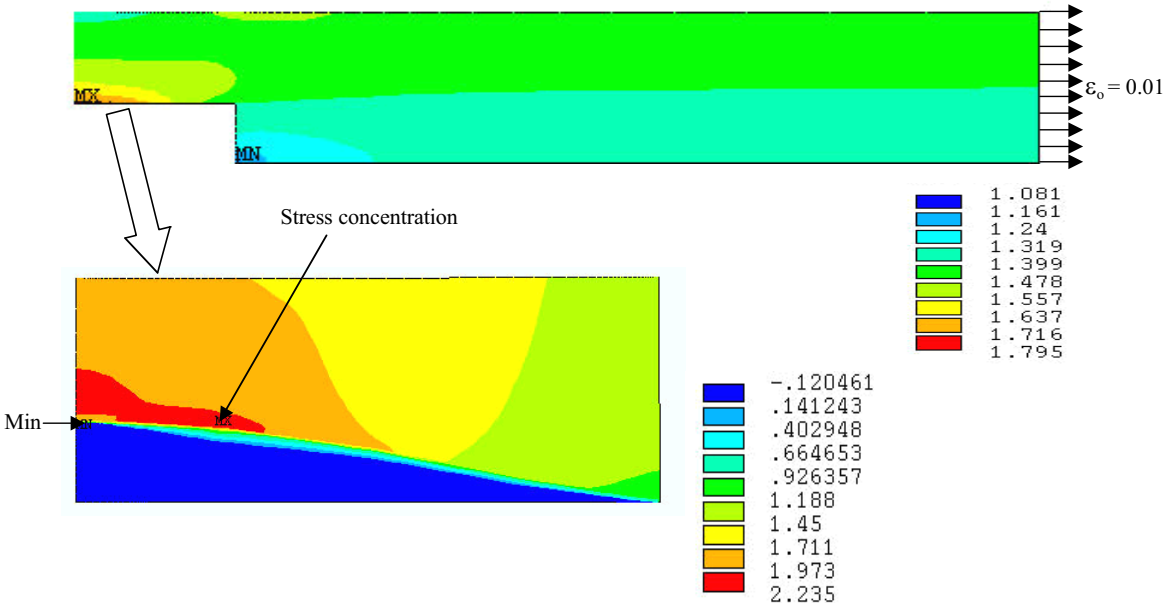

Figure 11 : Maximum principal (σ_1) stress contours (σ_o = 1.404 GPa, global and local views)

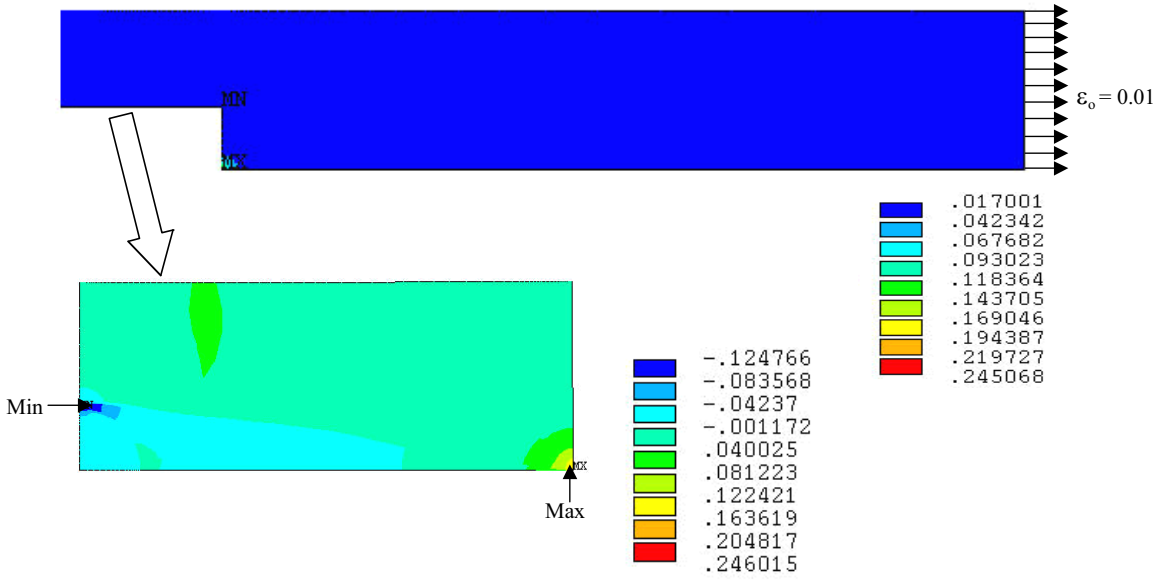

Figure 12 : Minimum principal (σ_2) stress contours (σ_o = 1.404 GPa, global and local views)

Table 2 : Stress concentration along x-and-y axes

	Stress concentration along y-axis*		Transverse stress concentration at A+
h_d/R_{FOS}	$K_I = \sigma_y/\sigma_o$	$K_t = \sigma_x/\sigma_o$	$K_{RP} = \sigma_y/\sigma_o$
2.50	-0.148	1.518	0.158
3.12	-0.165	1.443	0.171
4.00	-0.188	1.386	0.185
5.00	-0.212	1.358	0.196

* Interface between the optical fiber coating and the composite.
\+ Truly singular pointσ_o = 1.404 GPa

the applied average stress at x = L of 1.404 GPa. The stress concentration factor (σ_1/σ_0) is 1.59 at the location separating the composite and the resin pocket (see Fig. 11) and it is designated at location C. This value is not far from the stress concentration (1.71) calculated by Lekhnitskii's solution (See section 3.4) but at a different location. A high compressive stress occurs at the interface between the optical fiber and the composite on the y-axis. For compressive loading this stress reverses sign and becomes tensile. Therefore, under compression loading, interfacial failure could be a potential first failure owing to low transverse strength of the composite. This agrees with the hypothesis made in the previous section. The stress σ_2 is perpendicular to load or the reinforcing fiber access in most of the region. This stress is maximum at A. The stress concentration factor is about 0.171. This stress component is significant to cause transverse cracking because of very low transverse strength of the composite. This again agrees with the hypothesis for tensile loading. The stress concentrations at these critical locations are listed in Table 2. The table also includes solutions for different values of h_d. These contour plots confirm that critical stresses occur along x and y axes of the model. Hence stresses along these axes are examined for all cases.

7.1.2 Variation of σ_x and σ_y Stresses on x-axis

Figure 13 shows a plot of the normalized σ_x distribution along the x-axis. All σ_x stresses were extracted in ANSYS using path definition. All stresses are normalized by remote average stress (σ_o). As x approaches L (model length), σ_x approaches σ_o. At the root of the resin pocket, x = $8R_{FOS}$, σ_x jumps because the material stiffness changes from resin to composite. Results for both 8- and 12-ply laminates are compared in this figure and they are almost identical. This confirms that the present results are valid for other thicker laminates also.

Variation of σ_y along x is shown in Fig. 14. A sharp rise in stress occurs at x = R_{FOS} (interface between the fiber optics and resin) and $8R_{FOS}$. At x = $8R_{FOS}$ (the point A), σ_y stress shows a steep gradient, which is an indication of "singularity". This is due to the formation of a resin wedge at this location. In the geometric model the resin wedge angle used was 1^o. This high transverse stress ($0.171\sigma_0$) could cause fiber matrix split as the initial failure mode. The σ_y stress becomes zero away from the singular point, as expected. The average nodal value of σ_y stress at A is used for defining the stress concentration factor (K_{RP}) due to the resin pocket. However, this value may be different and probably a function of mesh refinement. The computed K_{RP} value is 0.171(see Table 2). Again, the difference between 8- and 12-ply laminates is very small or negligible. The stress distribution in Figs. 13 and 14 will be reversed for compressive loading, which will change the conclusion accordingly.

7.1.3 Variation of σ_x and σ_y Stresses on y-axis

Figure 15 shows the variation of the normalized σ_x stress along the y-axis. The stress, σ_x, jumps at the interface between the coating and the composite. It changes from compressive within the FOS to tensile outside the FOS. The peak value occurs just outside the resin and within the composite (point B). The stress concentration factor (K_{ty}) is 1.443 and it is less than the global stress concentration factor 1.59 which occurs at C between the resin pocket and the composite (see Fig. 11). This stress con-

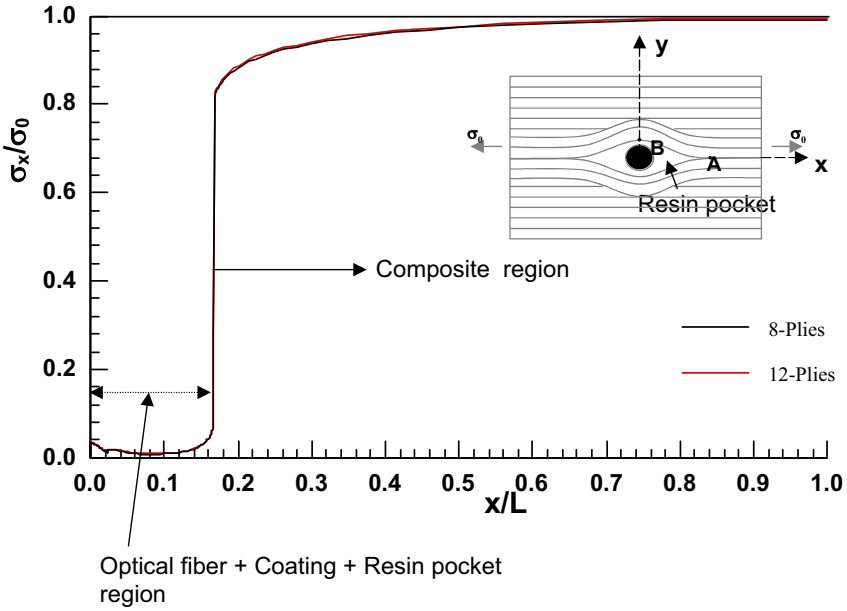

Figure 13 : Variation of σ_x along x-axis over the complete length

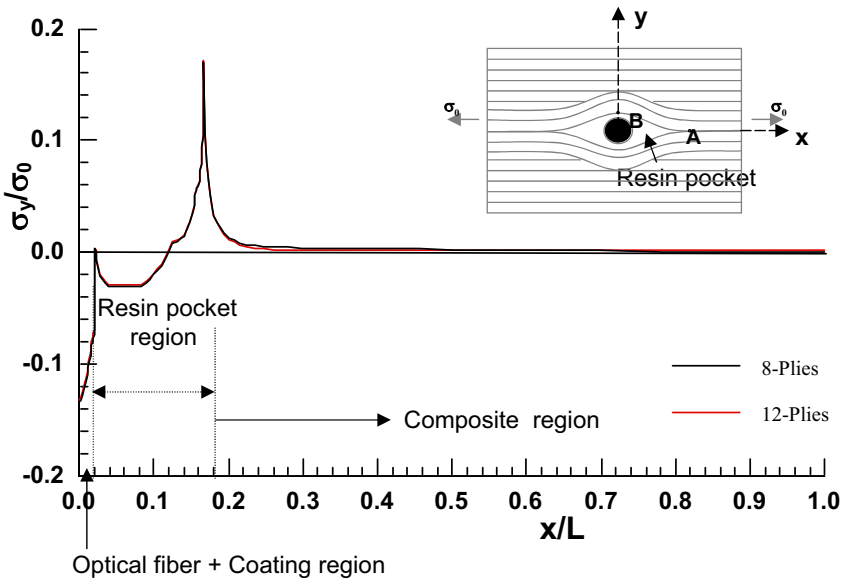

Figure 14 : Variation of σ_y along x-axis over the complete length

centration is the result of geometric disturbance of the reinforcing fiber due to embedment of optical fiber.

Figure 16 shows the variation of normalized σ_y stress along the y-axis. Under remote tensile loading, σ_y is compressive over a region $0 \leq y < 3R_{FOS}$ and changes to tensile outside this region. This stress concentration is referred to as the interfacial stress concentration factor (K_I) and it is about –0.165 for 12-ply and –0.17 for 8-ply laminate. Results show that K_I decreases with the increase in laminate thickness. The negative sign indicates that the σ_y stress will have the opposite sign of the applied stress. Therefore, under compression loading, σ_y is positive (tensile) and could cause interfacial cracking when it exceeds the transverse tensile strength of the composite.

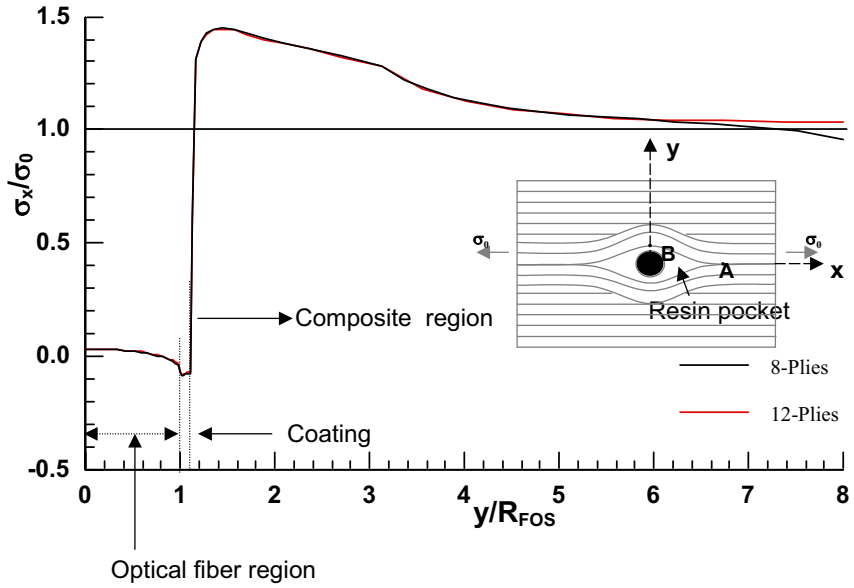

Figure 15 : Variation of σ_x along y-axis

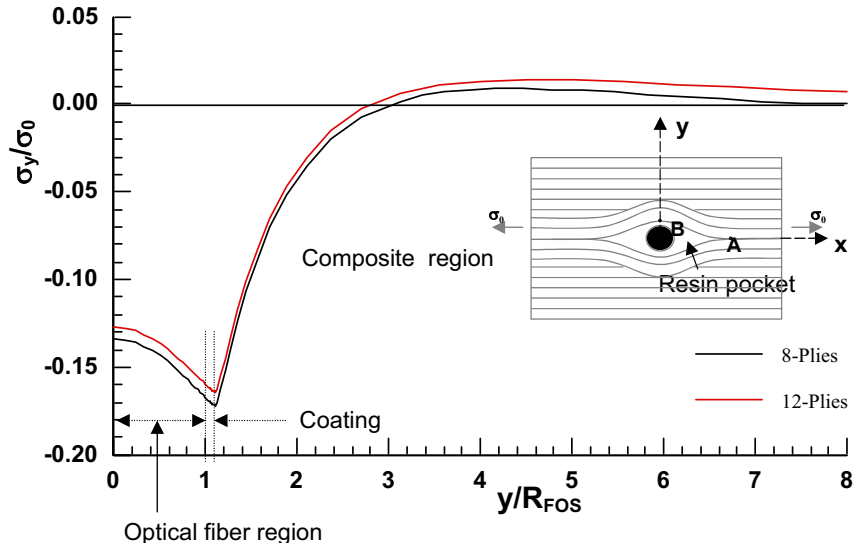

Figure 16 : Variation of σ_y along y-axis

7.2 Effect of Fiber Disturbance Height (h_d)

The effect of fiber disturbance height is investigated changing h_d/R_{FOS} values. Values of h_d/R_{FOS} selected are 2.5, 3.12 (baseline), 4 .0 and 5.0. The normalized stress distributions of σ_x and σ_y along the x- and y-axes are shown in Figs. 17 through 19 and the stress concentration values are listed in Table 2. The transverse stress concentration (K_{RP}) at resin pocket (A) increased with increase in h_d/R_{FOS}. The variation is within 15% of the baseline value. Similarly magnitude of K_I near B also increased with increase in h_d/R_{FOS}. This variation can be as high as 28% for h_d/R_{FOS}= 5. Axial stress concentration at B decreased with increase in h_d/R_{FOS}. However, this variation is less than 6% for the range of h_d/R_{FOS} investigated. In summary, a small variation of h_d/R_{FOS} from the baseline value will have less than 10% changes in SCF for all stresses.

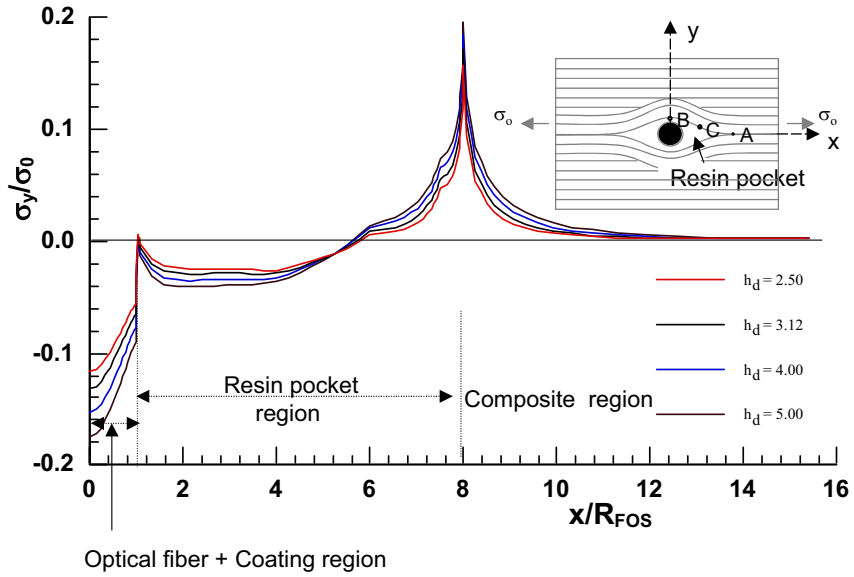

Figure 17 : Variation of Normalized σ_y along x-axis for various h_d/R_{FOS} values

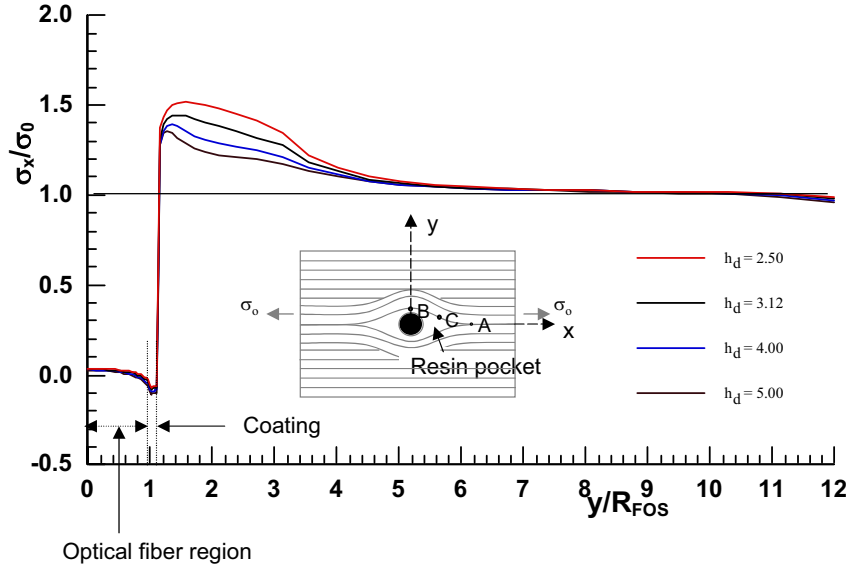

Figure 18 : Variation of Normalized σ_x along y-axis for various h_d/R_{FOS} values

7.3 Effect of Resin Pocket Length (L_{RP})

The effect of resin pocket length (L_{RP}) is investigated by changing L_{RP} from 4 to 12 R_{FOS}. For each case all stresses are normalized by the respective remote average stress values (σ_o), which are listed in Table 3. The trend in the stress plots remained similar to Figs. 17 through 19, except that the point A shifted with L_{RP}. The stress concentration at A (K_{RP}), interfacial stress concentration (K_I) at B, and the axial stress concentration (K_{ty}) near B within the composite are listed in Table 3. There was no measurable change in transverse stress concentration $K_{RP,}$ with change in L_{RP}.

K_{ty}, decreased with the increase in L_{RP} and so does the stress concentration factor (K_{tc}) at C. The interfacial stress concentration factor K_I, also decreased with increase in L_{RP}. K_{ty} and K_{tc} increased by 9.8% and 6.7%, respectively, as the L_{RP} values decreased from $8R_{FOS}$ to $4R_{FOS}$. The values of K_{ty} and K_{tc} decreased by 20%

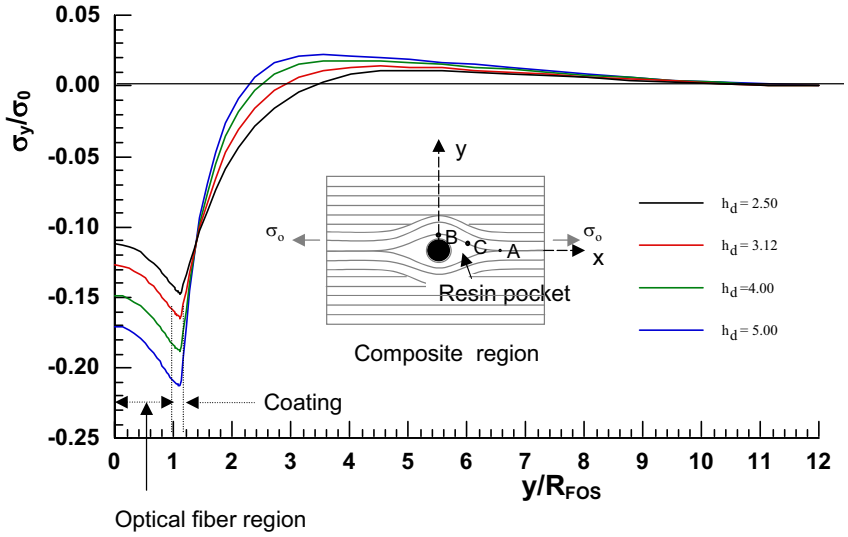

Figure 19 : Variation of Normalized σ_y along y-axis for various h_d/R_{FOS} values

Table 3 : Stress Concentration along x-and-y axes (L_{RP})

Resin Pocket Length, L_{RP}	Average Stress, σ_o GPa	Transverse Stress Concentration at A $K_{RP} = \sigma_y/\sigma_o$	Stress Concentration along y-axis $K_{ty} = \sigma_x/\sigma_o$	$K_I = \sigma_y/\sigma_o$	Stress Concentration at C $K_{tc} = \sigma_x/\sigma_o$
$4R_{FOS}$	1.404	0.169	1.589	-0.327	1.900
$6R_{FOS}$	1.404	0.170	1.555	-0.239	1.720
$8R_{FOS}$	1.404	0.171	1.447	-0.172	1.583
$10R_{FOS}$	1.400	0.172	1.386	-0.136	1.441
$12R_{FOS}$	1.395	0.173	1.350	-0.107	1.383

and 12.6% respectively as the L_{RP} values increased from $8R_{FOS}$ to $12R_{FOS}$. The L_{RP} value has a profound impact on the stress concentration factor, K_I, as it increased by 90% with the decrease in L_{RP} from $8R_{FOS}$ to $4R_{FOS}$ and decreased by 38% with the increase in L_{RP} from $8R_{FOS}$ to $12R_{FOS}$.

8 Effect of Curing Stresses on Stress Field

The composite AS4/3501-6 panels manufactured in the test program [Emmanwori (2002)] were cured at 350 ^oF and then cooled down to room temperature. As established in the literature, the first 100 ^oF of cool down has very little impact on the curing residual stresses because of high visco-elastic relaxation. Therefore, curing stresses induced from 250 ^oF to room temperature (75 ^oF) were calculated from the finite element analysis. All the material and thermal properties are listed in Tables 1a and 1b. Plot of curing stresses σ_y along x-axis and σ_x and σ_y along y-axis are shown in Figs. 20 and 21 respectively. All stresses are in GPa unit, since they cannot be normalized by mechanical components. Critical stresses at critical locations (A and B) are listed in Table 4. These stresses are far less than the composite AS4/3501-6 material strength (See Table 5).

9 Prediction of Failure Stress

From the stress concentration factors and the residual curing stresses reported in the previous section, one can derive the following failure equations including and not including the residual curing stresses for tension and compression loading cases. Failure criteria used are the maximum stress failure criteria. According to this theory failure occurs when at least one stress component along one of the principal material axes exceeds the corresponding strength in that direction. Accordingly, these criteria are defined as follows:

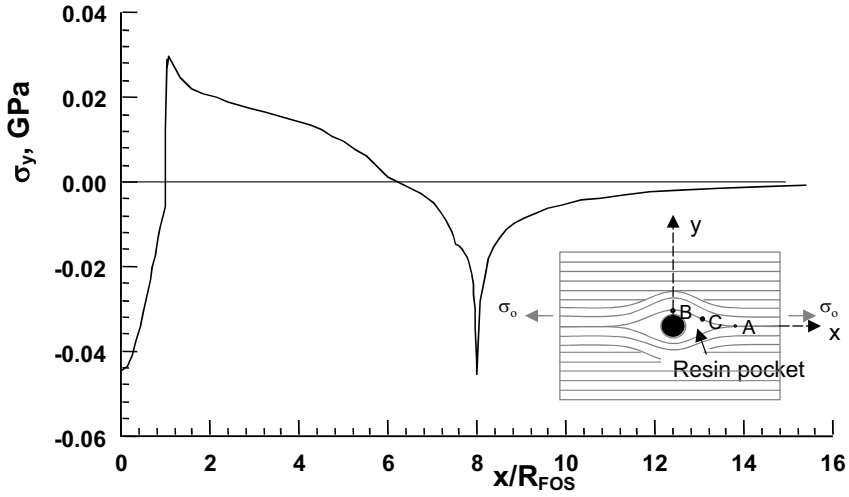

Figure 20 : Variation of σ_y along x-axis due to ΔT = -175 ^oF

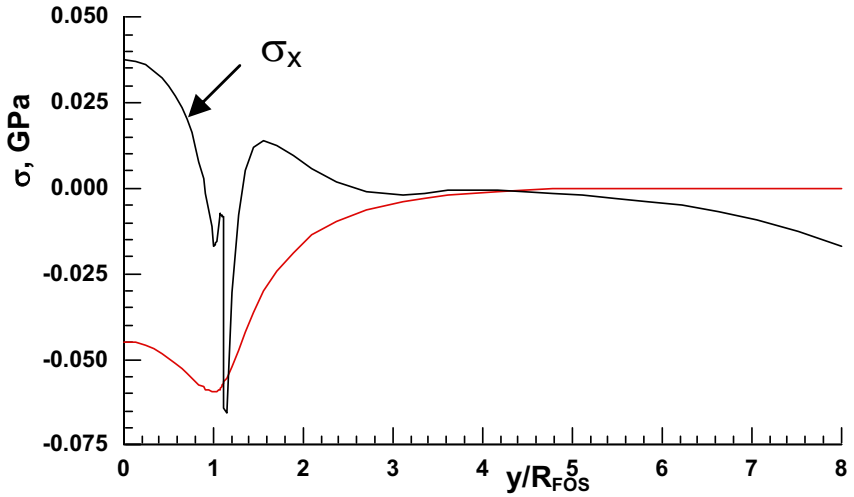

Figure 21 : Variations of σ_x and σ_y along y-axis due to ΔT = -175 ^oF

Tensile Stresses:

$\sigma_1 \geq F_{1t}$ Fiber Break

$\sigma_2 \geq F_{2t}$ Matrix Break

Compressive Stresses:

$\sigma_1 \leq F_{1C}$ Fiber Crushing

$\sigma_2 \leq F_{2C}$ Matrix Yielding

Shear Stresses:

$|\sigma_6| \geq F_6$ Shear Crack

The subscripts 1 and 2 refer to directions along and across reinforcing fibers, and refer to compression and tension loading respectively.

9.1 Tension Failure Load

Failure initiation and fracture stresses are:

$$\text{Initiation} = \frac{F_{2t}}{K_{RP}} \quad \text{OR} \quad \frac{F_{2t} - (\sigma_r)_{RP}}{K_{RP}}$$

$$\text{Final Fracture} = \frac{F_{1t}}{(K_{ty})_{@B}} \quad \text{OR} \quad \frac{F_{1t} - (\sigma_r)_{@B}}{(K_{ty})_{@B}}$$

The first part of each equation does not include residual curing stresses while the second part is including residual curing stresses.

Table 4 : Curing Stresses

Loading	Transverse stress at A	Stress along y-axis		Stress at C
	σ_y, GPa	σ_x, GPa	σ_y, GPa	σ_x, GPa
Curing Stresses	-0.046	-0.066	-0.060	0.039

Table 5 : Strength Properties for AS4/3501-6

Material Strength				
F_{1t} (GPa)	F_{2t} (MPa)	F_{1C} (GPa)	F_{2C} (MPa)	F_6 (MPa)
2.28	57.00	1.44	228.00	71.00

Table 6 : Failure Initiation Stresses when Curing Stresses are included

Type and location of failure		Failure Stress	
		Predicted	Experimental
Tension:	Initiation by fiber splitting at A	335 MPa	----
	Final fracture at B or C	1.407 GPa	1.84 GPa
Compression	Initiation by fiber splitting near	347.3 MPa	----
	Final fracture at B or C	0.825 GPa	0.737 GPa

9.2 Compression Failure Load

$$\text{Initiation} = \frac{F_{2t}}{K_I} \quad \text{OR} \quad \frac{F_{2t} - (\sigma_r)_I}{K_I}$$

$$\text{Final Fracture} = \frac{F_{1C}}{K_{t@BI}} \quad \text{OR} \quad \frac{F_{1C} - (\sigma_r)_{@B}}{K_{t@B}}$$

Using the above failure equations and the material strength in Table 5, tension and compression failure loads were predicted for the baseline case. This includes failure initiation and final fracture. Table 6 summarizes the results for both tension and compression loading.

For tension loading, the predicted initial failure stresses are 602 and 333 MPa with and without curing stresses respectively. The predicted final fracture stresses are 1.45 and 1.40 GPa, for cases with and without curing stresses respectively, while the measured strength was 1.84 GPa.

For compression loading, the predicted initial failure stresses are 684 and 331.4 MPa with and without curing stresses respectively. The predicted fracture stresses are 0.87 and 0.82 GPa, for cases with and without curing stresses respectively, while the measured strength was 0.74 GPa.

When the curing stresses are included, initial failure and final fracture stresses are very close to each other. Therefore, the possibility of distinguishing the failure initiation and final fracture would be very difficult. Even Jensen, Pascaul and August (1992), Mathews and Sirkis (1990) and Davidson (1992) could not clearly distinguish between the two failure modes.

10 Concluding Remarks

The fiber optic sensor (FOS) embedded perpendicular to reinforcing fibers causes an 'Eye' shaped defect. The length is about 16 times fiber optic radius (R_{FOS}) and height is $2R_{FOS}$. The eye contains fiber optics in the center surrounded by an elongated resin pocket. Embedding FOS caused geometric distortion of the reinforcing fiber over a half equal to 6 to 8 R_{FOS}. This defect causes severe stress concentration at the root of the resin pocket, the interface between the optical fiber and the composite, and at 90 ^{o} to load direction in the composite. The stress concentration was calculated by finite element modeling of the representative micrograph. The FE results agreed reasonably with analytical and experimental data in the literature for a similar problem. The stress concentration in axial direction was about 1.44, interfacial was -0.165 and resin pocket was 0.171. Under tensile loading, the

initial failure was by transverse matrix cracking (fiber splitting) at the root of the resin pocket leading to final fracture by fiber breakage. Under compression loading, the failure initiation was by interfacial cracking due to large transverse tensile stress and the final fracture was by compression. Stress analysis results agree with the hypothesis made. The parametric study of the geometric size of the defect showed that the length of the defect greatly alters the critical stresses. The residual curing stresses are significant enough to change the predicted strength of the composite. The fracture stresses calculated from the analysis using the maximum stress criteria agreed reasonably with test data in the literature.

Acknowledgement: The authors wish to thank the Offices of Naval Research for financial support through a grant N 00014-01-1-1033 and Dr. Yapa Rajapakse, Program manager for ship structures. The authors also wish to thank the North Carolina Super Computing Center, Research Triangle Park, NC for providing computational support.

References

ANSYS 5.6, Swanson Analysis System, Inc., Urbana, IL.

Budiansky, B. (1983): Micromechanics, *Computers and Structures*, Vol. 16, No.1, pp. 3-12.

Budiansky, B.; Fleck, N. A. (1993): Compressive Failure of Fibre Composites, *Journal of Mech. Phys. Solids*, Vol. 41, pp. 183-211

Carman, G. P.; Reifsneider, K. L. Analytical Minimization of the Obtrusive Behaviour Indicative of Embedded Sensors and Actuators, Recent Advances in Adaptive and Sensory Materials and Their Applications, Craig Rogers, Ed., Technomic Publishing, Lancaster, April 992, pp.314 – 331.

Claus, R. O.; Bennett, K. D.; Jackson, B. S. (1985): Nondestructive of Embedded Optical Fibers, *Review of Progress in Quantitative Nondestructive Evaluation*, Vol. 5b, pp. 1149-1156.

Czarnek, R.; Guo, Y. F.; Bennet, K. D.; Claus, R. O. (1989): Interferometric Measurements of Strain Concentrations Induced by an Optical FiberEmbedded in a Fiber Reinforced Composite, *Fiber Optic Smart Structures and Skins*, Vol. 986, SPIE, pp.43-54.

Dasgupta, A.; Wan, Y.; Sirkis, J. S.; Singh, H. (1990): Micro-Mechanical Investigation of an Optical Fiber Embedded in a Laminated Composite, *Fiber Optic Smart Structures and Skins III*, Vol. 1370, SPIE, 1990, pp.119-128.

Davidson, R. (1992): Do Embedded Sensor Systems Degrade Mechanical Performance of Host Composites? Active materials and Adaaptive Structures, G.J. Knowles, Ed., Institute of Physics Publishing, Philadelphia, pp.109-114.

Emehel, T. C.; Shivakumar, K. N. (1997): Tow Collapse Model for Compression Strength of Textile Composites, *Journal of Reinforced Plastics and Composites*, Volume 16, Number 1, pp.86-101.

Emmanwori, L. (2002): Intrusion of Embedded Fiber Optic Sensor on Structural Integrity of Composite Laminate, Ph.D Dissertation, NCA&T State University.

Emmanwori, L.; Shivakumar, K. N. (2002): Structural Performance of Composite Laminates with Embedded Fiber Optic Sensor Under Tension and Compression Loads, Proceedings of the 43^{rd} Annual Conference of American Institute of Aeronautics and Astronautics, Denver, CO.

Holl, M.; Boyd, S. (1993): The Effect of Embedded Fiber Optics on the Mechanical Properties of a Composite Host Material, *Smart Materials*, SPIE, Vol. 1916, pp. 109-117.

Jensen, D. W.; Griffiths, R. W. (1988): Optical Fiber Sensing Considerations for a Smart Aerospace Structure, Proceedings of Fiber Optics Smart Structures and Skins, SPIE, Boston, MA, September 8-9, pages 70-76.

Jensen, D.; Pascual, J.; August, A. (1992): Performance of Graphite/Bismaleimid laminates With Embedded Optical Fiber Optics, Part I: Uniaxial Tension, Smart Materials and Structures, 24-30.

Jensen, D.; Pascual, J.; August, A. (1992): Performance of Graphite/Bismaleimid laminates With Embedded Optical Fiber Optics, Part II: Uniaxial Compression, Smart Materials and Structures, 31-35.

Jensen, D. W.; Pascual, J.; August, J. A. (1992): Tensile Strength and Stiffness Reduction in Graphite/Bismaleimide Laminates with Embedded Fiber-Optic Sensors, *Active Materials and Adaptive Structures*, G.J. Knowles, Ed., Institute of Physics Publishing, Philadelphia, pp. 115-120.

Lekhnitskii, S.G. (1975): *Anisotropic Plates*, 2 edition,

Gordon and Breach Publishing.

Mathews, C. T.; Sirkis, J. S. (1990): The Interaction Mechanics of Interferometric Optical Fiber Sensors Embedded in a Monolithic Structure, *Fiber Optic Smart Structures and Skins III*, Vol. 1370, SPIE, pp.142-153.

Measures, R. M. (1989): Fiber optic smart structures program at UTIAS *Fiber Optic Smart Structure and Skins II*, SPIE Vol. 1170, pp. 92-108.

Pak, Y. E.; DyReyes, V.; Schmuter, E. S. (1992): Micromechanics of Fiber Optic Sensors, Active Materials and Adaptive Structures, G. J. Knowles, Ed., Institute of Physics Publishing, Philadelphia, pp.121-128.

Roberts, S. S.; Davidson, R. (1991): Mechanical Properties of Composite Materials Containing Embedded Fibre Optic Sensors, *Fiber Optic Smart Structures and Skins IV*, SPIE, Vol.1588, pp.326-341.

Roberts, S.; Davidson, R. (1992): Finite Element Analysis of Composite Laminates Containing Transversely Embedded Optical Fiber Sensors, First European Conference on Smart Structures and Materials, Glasgow.

Salehi, A.; Tay, A.; Wilson, D. A.; Smith, D. G. (1989): Strain Concentration Around Embedded Optical Fibers by FEM and Moire Interferometry, Design and Manufacturing of Advanced Composites, 5^{th} Conference, ASM International, Metals Park, OH, pp. 11-19.

Shelley, J. (1988): B. S. Thesis, The Pennsylvania State University.

Shivakumar, K. N.; Emmanwori, L. (2002): Mechanics of Failure of Embedded Fiber Optic Sensor in Composite Laminates Under tension and Compression loads, Proceedings of the 17^{th} Annual Conference of American Society for Composites, West Lafayette, IN

Udd, E.; Michal, S. E.; Higley, R. J.; Theriault, J. P.; LeCong, P.; Jolin, G. A.; Markus, A. M. (1987): Fiber-Optic Sensor Systems for Aerospace Applications, *Fiber Optic and Laser Sensors V*, Vol. 838, SPIE, pp. 162-168.

Verbis, J. T.; Tsinopoulos, S. V.; Polyzos, D. (2002): Elastic wave propagation in reinforced composite materials with non-uniform distribution of fibers, *CMES: Computer Modeling in Engineering & Sciences*, Vol. 3, No.6, pp. 803-814

Waite, S. R.; Sage, G. N. (1988): The Failure of Optical Fibres Embedded in Composite Materials, *Composites*, Vol. 19, No.4, 1988, pp. 288-294.

Yarcho, W. B. (1989): In-House Study to Determine the Effects of Embedded Optical Glass Fibers on the Strength of Graphite Composite Material, *Materials & Processes Report MoP-89-Jan-FDBC-006*, Wright Laboratory, Wright-Patterson AFB

A fiber-optic sensor is a sensor that uses optical fiber either as the sensing element ("intrinsic sensors"), or as a means of relaying signals from a remote sensor to the electronics that process the signals ("extrinsic sensors"). Fibers have many uses in remote sensing. Depending on the application, fiber may be used because of its small size, or because no electrical power is needed at the remote location, or because many sensors can be multiplexed along the length of a fiber by using light Structures embedded with fiber optic sensor are considered as primary sensing candidates for smart structures to. monitor a wide range of physical quantities such as strain, temperature. Although optical fibers have small.Â concentration in the vicinity of the embedded optical fiber. Benventiste et al. 1989 predicted the stress field in.Â resin pocket geometry for stress analysis of optical fiber embedded in laminates composites. Dasgupta and Sirkis. 1992 showed that strain concentrations near an embedded optical fiber are highly dependent on the thickness and. material properties of the coating. Case and Carman 1994 studied the compression strength of composites.